

PAPER • OPEN ACCESS

Nonlinear localized modes in two-dimensional hexagonally-packed magnetic lattices

To cite this article: Christopher Chong *et al* 2021 *New J. Phys.* **23** 043008

View the [article online](#) for updates and enhancements.



PAPER

Nonlinear localized modes in two-dimensional hexagonally-packed magnetic lattices

OPEN ACCESS

RECEIVED

17 September 2020

REVISED

29 December 2020

ACCEPTED FOR PUBLICATION

13 January 2021





PUBLISHED

5 April 2021

Original content from
this work may be used
under the terms of the
[Creative Commons
Attribution 4.0 licence](#).

Any further distribution
of this work must
maintain attribution to
the author(s) and the
title of the work, journal
citation and DOI.



Christopher Chong^{*,1} , Yifan Wang^{2,3} , Donovan Maréchal², Efstathios G Charalampidis⁴ , Miguel Molerón⁵, Alejandro J Martínez^{6,7}, Mason A Porter⁸ , Panayotis G Kevrekidis⁹  and Chiara Daraio²

¹ Department of Mathematics, Bowdoin College, Brunswick, ME 04011, United States of America

² Division of Engineering and Applied Science California Institute of Technology Pasadena, CA 91125, United States of America

³ School of Mechanical and Aerospace Engineering, Nanyang Technological University, Singapore, Singapore 639798

⁴ Mathematics Department, California Polytechnic State University, San Luis Obispo, CA 93407-0403, United States of America

⁵ Institute of Geophysics, Department of Earth Sciences, ETH Zurich, 8092 Zurich, Switzerland

⁶ Computational Biology Laboratory, Fundación Ciencia & Vida, Santiago, 7780272, Chile

⁷ Universidad San Sebastian, Santiago, 7510156, Chile

⁸ Department of Mathematics, University of California, Los Angeles, CA 90095, United States of America

⁹ Department of Mathematics and Statistics, University of Massachusetts, Amherst, MA, 01003, United States of America

* Author to whom any correspondence should be addressed.

E-mail: cchong@bowdoin.edu

Keywords: breather, Fermi–Pasta–Ulam–Tsingou lattice, magnetic lattice, hexagonal lattice, nonlinear localized mode

Abstract

We conduct an extensive study of nonlinear localized modes (NLMs), which are temporally periodic and spatially localized structures, in a two-dimensional array of repelling magnets. In our experiments, we arrange a lattice in a hexagonal configuration with a light-mass defect, and we harmonically drive the center of the chain with a tunable excitation frequency, amplitude, and angle. We use a damped, driven variant of a vector Fermi–Pasta–Ulam–Tsingou lattice to model our experimental setup. Despite the idealized nature of this model, we obtain good qualitative agreement between theory and experiments for a variety of dynamical behaviors. We find that the spatial decay is direction-dependent and that drive amplitudes along fundamental displacement axes lead to nonlinear resonant peaks in frequency continuations that are similar to those that occur in one-dimensional damped, driven lattices. However, we observe numerically that driving along other directions results in asymmetric NLMs that bifurcate from the main solution branch, which consists of symmetric NLMs. We also demonstrate both experimentally and numerically that solutions that appear to be time-quasiperiodic bifurcate from the branch of symmetric time-periodic NLMs.

1. Introduction

Discrete breathers are spatially localized, time-periodic solutions of nonlinear lattice differential equations. They have been studied in a host of scientific problems, including optical waveguide arrays and photorefractive crystals [1], Josephson-junction ladders [2, 3], layered antiferromagnetic crystals [4, 5], halide-bridged transition-metal complexes [6], dynamical models of the DNA double strand [7], molecular lattices [8], Bose–Einstein condensates in optical lattices [9], and many others.

Most of the immense volume of work—now spanning more than three decades—on discrete breathers has been in one-dimensional (1D) lattices [10–12]. Most relevant to the present article is research on discrete breathers in Fermi–Pasta–Ulam–Tsingou (FPUT) lattices, which have nonlinear inter-site coupling [13, 14]. FPUT-like lattices with power-law potentials have been used to model a variety of mechanical systems, such as granular crystals [15–18] and (more recently) magnetic lattices [19–21].

There have also been some studies of breathers in two-dimensional (2D) lattices, although there are many fewer such studies than there have been of breathers in 1D lattices. There are even fewer studies of

in-plane breathers [22]. Example 2D physical settings in which breathers have been examined include crystal lattices [12, 23], electric circuits [24], and dusty plasmas [25, 26]. Breathers in 2D lattices have been analyzed with both asymptotic methods [27] and numerical methods in both homogeneous [22, 28] and heterogeneous media [29, 30]. See [8, 31] for overviews of results about 2D discrete breathers.

The 2D setting of the present work is a mechanical system in which each magnet has two in-plane displacement fields, which distinguishes it from many studies of scalar 2D lattices, such as those that describe electrical circuits [24]. Specifically, we examine a lattice of repelling magnets that are arranged in a hexagonal configuration. The choice of a hexagonal arrangement is motivated by our experimental setup, as hexagonal configurations are more robust structurally than other arrangements (such as square configurations). At the center of the lattice, there is a light-mass defect, which introduces a localized defect mode into the spectrum of the linearization of the system. To excite the system experimentally, we drive the center of the lattice by a force. This force arises from the current that flows along a wire that we suspend above the lattice. We model damping using a dashpot term. Putting everything together, the proposed model for our experimental setup is a damped, driven variant of a vector FPUT lattice.

Although a breather is defined as a spatially localized and time-periodic structure, it is useful to label different types of breathers. Linear systems with an impurity or a defect (e.g. with a particle of lighter mass than the other particles) have isolated points in their spectra that lie above the spectral edge. We use the term ‘defect modes’ for the associated localized modes [32]. In the presence of nonlinearity, breathers can bifurcate from these modes and can exist for frequencies other than the linear defect frequency. We study such breathers in the present work, and we use the term ‘nonlinear localized modes’ (NLMs) [33] for breathers that manifest in this way. (Such solutions have also been called ‘defect breathers’ in other settings [34].) By contrast, we use the term ‘intrinsic localized modes’ (ILMs) for breathers that do not manifest via a defect or an impurity. One way for ILMs, which we do not investigate in the present paper, to manifest is via a modulational instability of plane waves [10]. In addition to breathers, other kinds of orbits—such as quasiperiodic and chaotic ones—can also occur in nonlinear lattices. For example, such orbits have been identified in strongly nonlinear damped, driven granular chains [35, 36], suggesting that such solutions may also be present in damped, driven magnetic lattices. In the present work, we examine such NLM states, their stability, and the modes that arise as a result of instabilities.

Our paper proceeds as follows. We present our experimental setup in section 2, and we detail the corresponding model equations, linear theory, and numerical methods in section 3. We give our main numerical and experimental results in section 4, where we explore NLM profiles, spatial decay, parameter continuations, and nearly time-quasiperiodic orbits. We conclude and discuss future challenges in section 5.

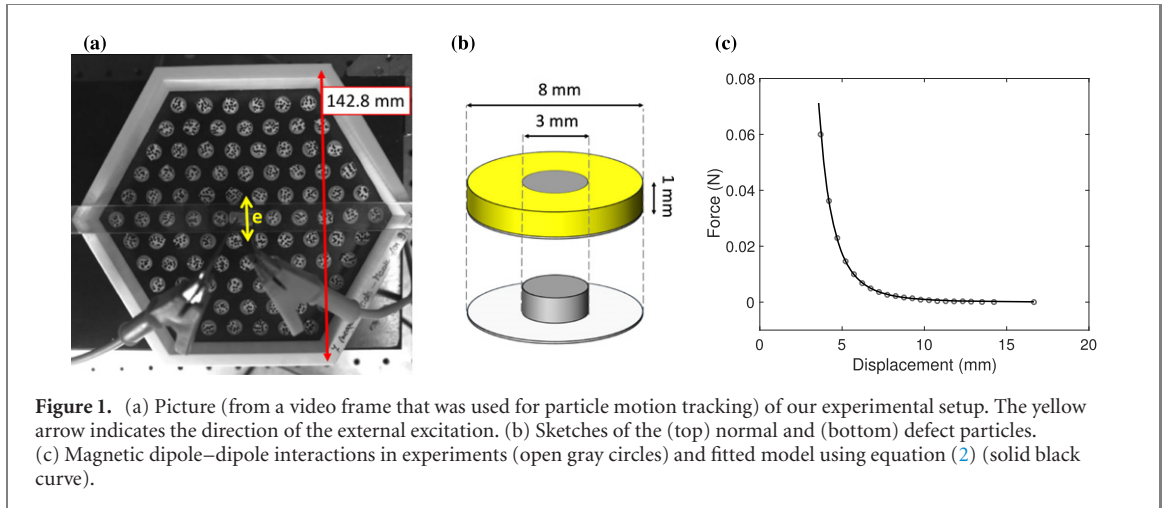
2. Experimental setup

We place a 2D lattice of magnetic particles on an air-bearing table to make the particles (i.e. the nodes of the lattice) levitate. The lattice consists of 127 magnetic particles that are hexagonally packed. We glue 36 of these particles to the boundaries, and 91 of them are free to move (see figure 1(a)). Each particle is a 3D-printed disk with a hole in the center, where we attach a neodymium magnetic cylinder. We glue a thin piece of cover glass at the bottom to make the surface smoother and thereby improve the levitation of the particles. We build the defect particle, which is located in the center of the lattice, by directly attaching the magnet on the glass without the 3D-printed structure. This particle has a lighter mass and serves as a defect (see figure 1(b)). The mean mass of a normal disk particle is $138.2 \text{ mg} \pm 3.1 \text{ mg}$ (where we measure the standard deviation from a sample of 20 particles). The defect particle has a mass of 81.6 mg, which corresponds to 58.68% of the normal particle mass.

We excite the defect particle using an external magnetic field that we generate using a conductive wire that we place over the particle at a height of 3 mm. We generate the AC current that flows through the wire from a lock-in amplifier (an SR860 500 kHz DSP lock-in amplifier), and we amplify it with an audio amplifier (Topping TP22, class D). The equation that describes the force that the wire exerts on a magnet that is a distance r from it is

$$F_{\text{wire}}(r) = \frac{I\mu_0\mathcal{M}}{2\pi} \frac{h^2 - r^2}{(h^2 + r^2)^2}, \quad (1)$$

where h is the height of the wire from the plane of floating disks, I is the wire current, $\mu_0 = 4\pi \times 10^{-7} \text{ N A}^{-2}$ is the magnetic permeability, and $\mathcal{M} = 7.8 \times 10^{-3} \text{ A m}^2$ is the magnetic moment of the floating disk. See the appendix for the derivation of equation (1). We use harmonic excitations in our experiment, so the current through the wire is $I(t) = aI_0 \sin(2\pi ft)$, where f is the drive frequency (in Hz), a is the drive-voltage amplitude (in volts), and $I_0 = 0.1 \text{ A V}^{-1}$ is the current per unit voltage that we measure in the wire.



The magnets repel each other. In the ideal situation of a perfect dipole–dipole interaction, the magnetic force between two repelling magnets is

$$F_{\text{magnet}}(r) = Ar^p, \quad (2)$$

where r is the distance (in meters) between the two center points of the magnets, $p = -4$, and $A = 3\mu_0\mathcal{M}^2/2\pi$. Although equation (2) is reasonable for large separation distances with the given ideal values of A and p , we obtain better agreement by empirically determining A and p . Because the force between two magnetic dipoles is too small to measure directly, we create a pair of plastic plates, with 25 magnets attached to each plate. We position the plates to align each pair of cylindrical magnets from opposite plates through their radial directions. We measure the repulsive force as a function of the displacement between these two plates in a materials tester (Instron ElectroPuls E3000). The distance between the magnets on each plate is large enough (specifically, it is 2.5 cm) so that we can neglect interactions between magnets that are not aligned. The distance between a magnet on the first plate and the non-aligned magnets on the other plate is larger than 25 mm. As one can see in figure 1(c), the interaction force already approaches 0 for distances that are significantly smaller than 25 mm. Consequently, the measured force is approximately equal to the sum of the repulsive forces of the 25 isolated magnet pairs. We fit the data using equation (2), which yields $p \approx -4.2$ and $A \approx 3.8 \times 10^{-12} \text{ N/m}^p$ (see figure 1(c)).

We monitor the motion of the center particle using a laser vibrometer (Polytec CLV-2534), and we record the dynamics of the rest of the lattice using a digital camera (Point Gray GS3-U3-41C6C-C) with a frame rate of 90 fps. We analyze the images using digital-image-correlation (DIC) software (VIC-2D) to determine each particle's velocity. We inspect half of the lattice, as the cables that are connected to the driving wire block most of the system's other half (see figure 1(a)). Due to imperfections at the bottom of the glass disks (e.g. dust, scratches, and so on) and the fact that mass is not distributed evenly on a disk, a few particles start to rotate when they are levitated by the air that flows out of the air-bearing table. The DIC software then loses track of them. We ignore these rotating disks in our subsequent analysis. To estimate the value of the damping coefficient γ of a linear dashpot term, we excite the center particle in the lattice and let the resulting temporal amplitude decay to rest once we switch off the excitation. We then perform a linear regression on the logarithm of the amplitude to obtain an estimate for the decay rate β , where we are assuming an exponential decay that is proportional to $e^{\beta t}$. We then choose γ by minimizing the objective function $|\beta - \beta_r(\gamma)|$, where $\beta_r(\gamma)$ is the real part of the eigenvalue that is associated with the defect mode of the linear system with damping but no driving. (See equations (12, 13) with $a = 0$.) We do this because the linear defect mode in the damped, undriven system decays exponentially to 0 with a rate of $\beta_r(\gamma)$. This procedure yields $\gamma \approx 10.52 \times 10^{-3} \text{ N s m}^{-1}$. The lattice particles are always in motion with at least small speeds, even in the absence of excitation. This is due to interactions with the air flow from the table and imperfections (e.g. nonaxisymmetric mass distributions) of the particles. We use this motion to estimate the noise in the system. To evaluate the amount of noise, we record the lattice motion without excitation as a comparison; see the appendix for details about our noise estimation. We summarize the values of our measured and fitted parameters in table 1.

Table 1. Summary of the measured and fitted parameter values in our experimental setup.

Description	Symbol	Value (measured)	Description	Symbol	Value (fitted)
Mass of a bulk magnet	M_b	138.2 mg	Magnetic coefficient	A	3.8×10^{-12} N/m ^{p}
Defect mass	M_δ	81.6 mg	Nonlinearity exponent	p	-4.2
Static-equilibrium distance	δ	13.7 mm	Damping coefficient	γ	10.52×10^{-3} N s m ⁻¹
Wire height	h	3 mm	Magnetic moment	\mathcal{M}	7.8×10^{-3} A m ²

3. Theoretical setup

3.1. Model equations

Our goal is to study NLMs in a 2D hexagonal lattice. In selecting equations to model the system that we described in section 2, we seek the simplest possible model that incorporates the ingredients (nonlinearity, discreteness, and appropriate dimensionality) that are essential for NLMs and also yield reasonable agreement with experimental data. It is in this spirit that we develop our model equations. After doing so, we briefly discuss model simplifications.

We consider a hexagonally-packed lattice of magnets. We use the lattice basis vectors $\mathbf{e}_1 = (1, 0)$ and $\mathbf{e}_2 = (1/2, \sqrt{3}/2)$. Let $\mathbf{q}_{m,n}(t) = (x_{m,n}(t), y_{m,n}(t)) \in \mathbb{R}^2$ denote the displacement from the static equilibrium of the magnet at position $\mathbf{p} = \delta(m\mathbf{e}_1 + n\mathbf{e}_2)$ in the plane (see figure 2(a)), where δ is the center-to-center distance between two particles at static equilibrium. The lattice indices m and n take the values $\{-w, -(w-1), \dots, 0, \dots, w-1, w\}$, where w is the number of magnets along an edge of the hexagon. The lattice boundary is given by the hexagon with magnets at positions $(w\delta \cos(j\pi/3), w\delta \sin(j\pi/3))$, where $j \in \{0, 1, \dots, w-1\}$ (see figure 2(b)). For our fixed boundary conditions along the edge of the hexagonal boundary, $\mathbf{q}_{m,n}(t) = 0$ if $|m+n| > w$.

One can express the distance between the magnet with index (m, n) and one of its nearest neighbors in terms of the displacements $x_{m,n}$ and $y_{m,n}$ of the magnets from their respective static-equilibrium positions. Once we determine this distance, we compute the resulting force using equation (2). Summing the forces from each of the six nearest neighbors and applying Newton's second law leads to the following equations of motion:

$$M_{m,n}\ddot{\mathbf{q}}_{m,n} = -\mathbf{F}_0(\mathbf{q}_{m+1,n} - \mathbf{q}_{m,n}) - \mathbf{F}_1(\mathbf{q}_{m,n+1} - \mathbf{q}_{m,n}) + \mathbf{F}_{-1}(\mathbf{q}_{m,n} - \mathbf{q}_{m-1,n+1}) \\ + \mathbf{F}_0(\mathbf{q}_{m,n} - \mathbf{q}_{m-1,n}) + \mathbf{F}_1(\mathbf{q}_{m,n} - \mathbf{q}_{m,n-1}) - \mathbf{F}_{-1}(\mathbf{q}_{m+1,n-1} - \mathbf{q}_{m,n}) - \gamma\dot{\mathbf{q}}_{m,n} + \mathbf{F}_{m,n}^{\text{ext}}(t). \quad (3)$$

The vector functions $\mathbf{F}_j(\mathbf{q}) = \mathbf{F}_j(x, y) \in \mathbb{R}^2$ have magnitudes of

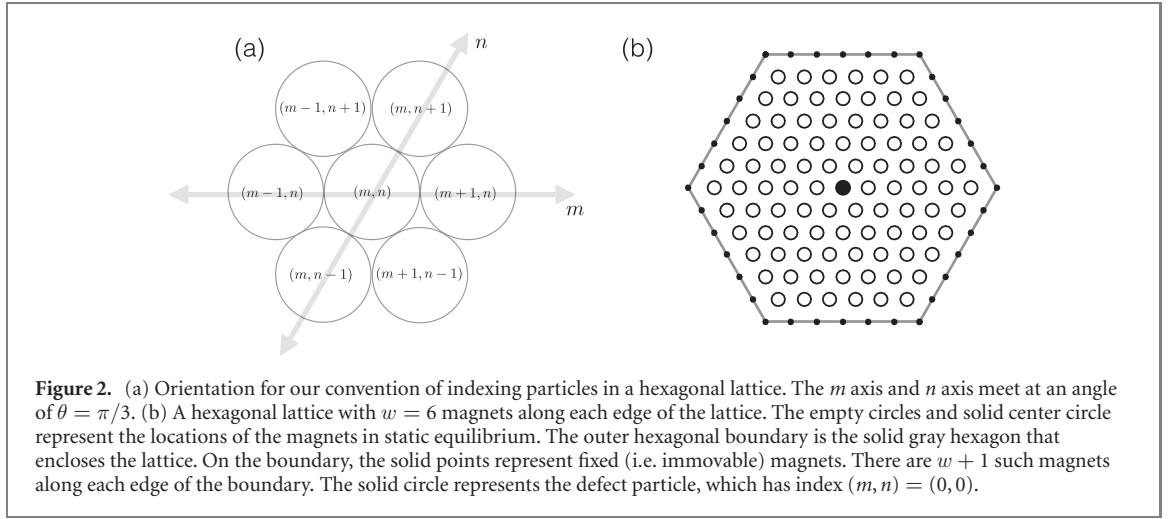
$$|\mathbf{F}_j(x, y)| = A \left[\sqrt{(\delta \cos(\theta_j) + x)^2 + (\delta \sin(\theta_j) + y)^2} \right]^p, \quad \theta_j = \frac{j\pi}{3}, \quad j \in \{-1, 0, 1\},$$

and their directions are given by the relative displacement vector $(\delta \cos(\theta_j) + x, \delta \sin(\theta_j) + y)$. The mass of the magnet with index (m, n) is $M_{m,n}$. The dashpot term $\gamma\dot{\mathbf{q}}_{m,n}$ is a phenomenological term that we add to account for damping. Using such a term has yielded reasonable agreement with experiments in other, similar lattices [19, 37, 38]. The quantity $\mathbf{F}_{m,n}^{\text{ext}}$ is the external force that we apply to the magnet at (m, n) . In the present article, we consider excitations via a wire that is directly above the center of the lattice. The magnitude of the excitation is given by equation (1). Therefore,

$$\mathbf{F}_{0,0}^{\text{ext}}(t) = a \sin(2\pi ft) \frac{I_0 \mu_0 \mathcal{M}}{2\pi} \begin{pmatrix} \cos(\phi) \frac{h^2 - x_{0,0}^2}{(h^2 + x_{0,0}^2)^2} \\ \sin(\phi) \frac{h^2 - y_{0,0}^2}{(h^2 + y_{0,0}^2)^2} \end{pmatrix}, \quad (4)$$

where ϕ is the angle of the excitation and $\mathbf{F}_{m,n}^{\text{ext}} = 0$ when $m \neq 0$ and $n \neq 0$. In our experiments and in most of our numerical computations, the excitation angle is $\phi = \pi/2$, so we excite only the y -component of the center magnet. We will also explore some other excitation angles. As we discuss in the appendix, the lattice forces dominate the dynamics. The wire has only a small effect on magnets other than the one in the center of the lattice. For example, at static equilibrium, the force that is exerted on the center magnet by the wire is two orders of magnitude larger than the force that the wire exerts on the center magnet's nearest neighbors. Compare the results of inserting $r = 0$ and $r = \delta$ into equation (1).

In our model, we ignore effects beyond nearest-neighbor coupling of the magnetic interactions. It is known that such long-range effects can alter the structure of localized modes. For example, it was shown in [39] that the spatial decay of breathers can transition from exponential spatial decay to algebraic decay in lattices with algebraically decaying interaction forces (as is the case in our model) for lattices with



sufficiently many sites. More recently, Molerón *et al* [38] studied NLMs in a 1D magnetic lattice using a model with long-range interactions. Although the differences between long-range and nearest-neighbor lattices that were considered in [38] are detectable, they are still small. For example, at static equilibrium, the force that is exerted on the center magnet by its nearest neighbors is one order of magnitude larger than that exerted by its next-nearest neighbor. Compare the results of inserting $r = \delta$ and $r = 2\delta$ into equation (2). To keep our model as simple as possible, we ignore such small long-range effects.

In our analysis of experimental data, we ignore magnets that are rotating, so our model does not account for rotation. This leaves air resistance as the primary source of damping. Given the size of the magnets and velocities that we consider, we employ a linear dashpot [40]. We also assume that the magnets stay in a plane. We evaluate the many assumptions that we made in formulating the model in equation (3) via a direct comparison with experimental results in section 4.

For the remainder of the manuscript, we fix all parameters of the model (and we summarize them in table 1), except for the excitation amplitude a , frequency f , and angle ϕ . We will specify these in our various examples. In all cases, we examine a lattice with a single defect particle in the center and a hexagonal boundary with a length of $w = 6$ magnets (see figure 2). Importantly, we do not fit the parameter values to the reported experimental results. Instead, we determine them beforehand using the procedures that we detailed in section 2.

3.2. Linear analysis

We start with the basic linear theory of localized modes for our hexagonal magnetic lattice. We are particularly interested in modes with frequencies that lie above the cutoff frequency of the pass band. We first derive an analytical expression for the cutoff frequency, which is straightforward for an infinite-dimensional Hamiltonian system (i.e. with all integers m and n , along with $a = 0$ and $\gamma = 0$). We then numerically estimate the frequency of a linear mode that is associated with the defect in the associated finite-dimensional Hamiltonian system. Finally, we compute linear localized modes in the associated finite-dimensional damped, driven system.

Assuming small strains, such that

$$\frac{|\mathbf{q}_{m\pm 1,n} - \mathbf{q}_{m,n}|}{\delta} \ll 1, \quad \frac{|\mathbf{q}_{m,n\pm 1} - \mathbf{q}_{m,n}|}{\delta} \ll 1, \quad \frac{|\mathbf{q}_{m\pm 1,n\mp 1} - \mathbf{q}_{m,n}|}{\delta} \ll 1, \quad (5)$$

we Taylor expand to obtain

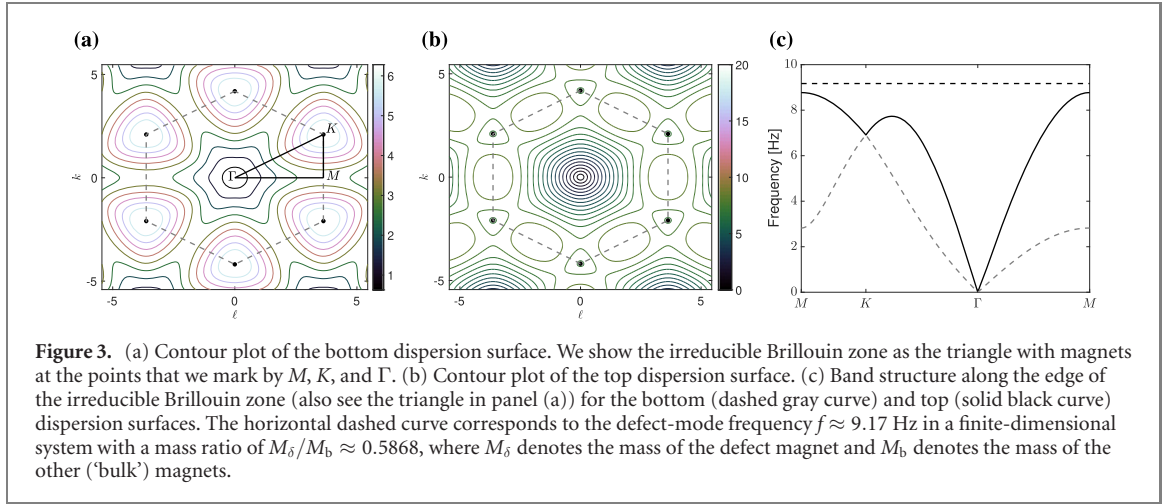
$$\mathbf{F}_j(\mathbf{q}) \approx \mathbf{F}_j(\mathbf{q}_0) + D\mathbf{F}_j(\mathbf{q}_0)\mathbf{q},$$

where $D\mathbf{F}_j$ is the Jacobian matrix of \mathbf{F}_j . Using this notation, the linearized equations of motion are

$$\begin{aligned} M_{m,n}\ddot{\mathbf{q}}_{m,n} = & -D\mathbf{F}_0(\mathbf{q}_{m+1,n} + \mathbf{q}_{m-1,n}) - D\mathbf{F}_1(\mathbf{q}_{m,n+1} + \mathbf{q}_{m,n-1}) \\ & - D\mathbf{F}_{-1}(\mathbf{q}_{m-1,n+1} + \mathbf{q}_{m+1,n-1}) + 2(D\mathbf{F}_0 + D\mathbf{F}_1 + D\mathbf{F}_{-1})\mathbf{q}_{m,n}, \end{aligned} \quad (6)$$

where

$$D\mathbf{F}_j = \begin{pmatrix} a_j & b_j \\ c_j & d_j \end{pmatrix}, \quad j \in \{-1, 0, 1\},$$



with

$$\begin{aligned}
 a_{-1} &= p\hat{\delta}, & b_{-1} &= 0, & c_{-1} &= 0, & d_{-1} &= \hat{\delta}, \\
 a_0 &= \frac{3+p}{4}\hat{\delta}, & b_0 &= \frac{\sqrt{3}(p-1)}{4}\hat{\delta}, & c_0 &= b_0, & d_0 &= \frac{1+3p}{4}\hat{\delta}, \\
 a_1 &= a_0, & b_1 &= -b_0, & c_1 &= -c_0, & d_1 &= d_0,
 \end{aligned}$$

and $\hat{\delta} \equiv A\delta^{p-1}$. For a monoatomic system (in which all magnets are identical, such that $M_{m,n} = M_b$), the linear system has plane-wave solutions

$$\mathbf{q}_{m,n} = \mathbf{q}_0 \exp\left(i(km + \frac{n}{2}(k + \sqrt{3}\ell))\right) e^{i\omega t}, \quad \mathbf{q}_0 \in \mathbb{C}^2, \quad k, \ell, \omega \in \mathbb{R},$$

where the wavenumbers k, ℓ and angular frequency $\omega = \omega(k, \ell)$ satisfy the dispersion relationship

$$[\omega(k, \ell)]^2 = \frac{\omega_a + \omega_d \pm \sqrt{(\omega_a + \omega_d)^2 - 4(\omega_a\omega_d - \omega_b\omega_c)}}{2}, \quad (7)$$

with

$$\omega_\alpha(k, \ell) = (-2\alpha_{-1} \cos(k) - 2\alpha_0 \cos(k/2 + (\sqrt{3}/2)\ell) - 2\alpha_1 \cos(k/2 - (\sqrt{3}/2)\ell) + 2(\alpha_{-1} + \alpha_0 + \alpha_1))/M_b$$

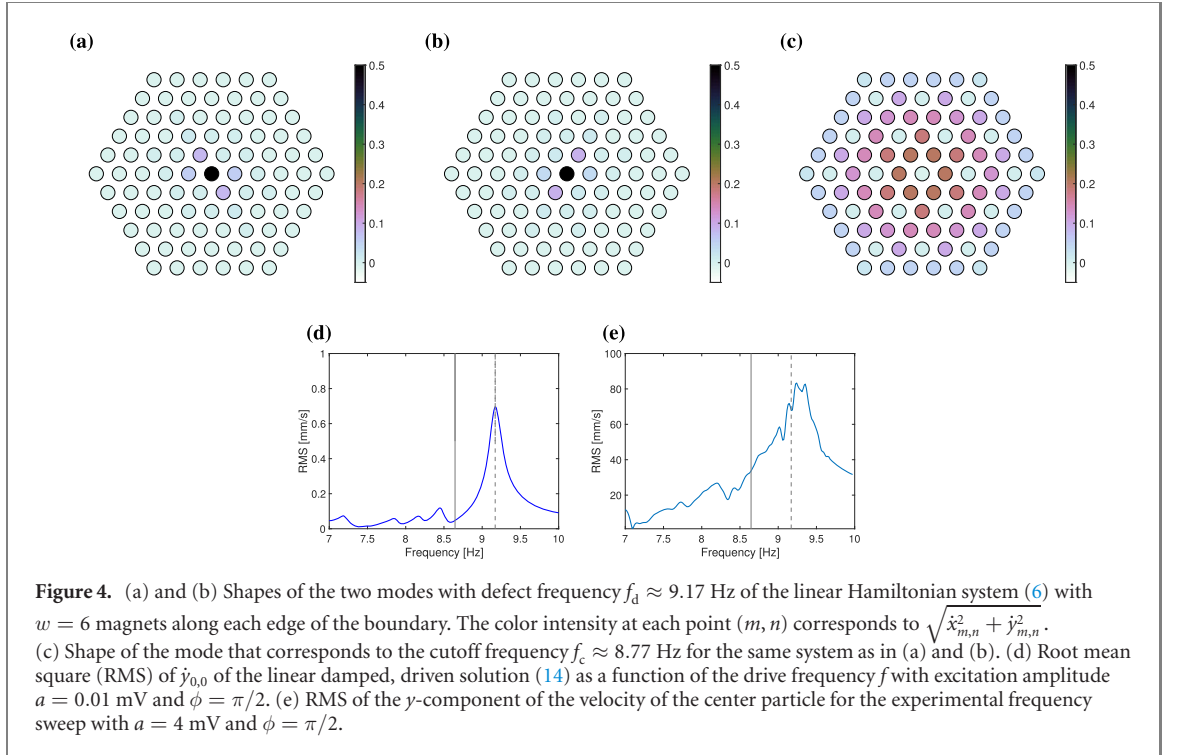
and coefficients $\alpha_j \in \{a_j, b_j, c_j, d_j\}$ (with $j \in \{-1, 0, 1\}$). In figures 3(a) and 3(b), we show contour plots of the two dispersion surfaces from equation (7). In figure 3(c), we show the dispersion curves along the edge of the irreducible Brillouin zone. The cutoff value of the pass band has the wavenumber pair $(k, \ell) = (0, 2\pi/3)$, which is where the dispersion curve attains its maximum value. For the parameter values in table 1, the cutoff frequency is $f_c = \omega_+(0, 2\pi/3)/(2\pi) \approx 8.77$ Hz, where ω_+ corresponds to the top dispersion surface.

The presence of the lighter defect introduces a linear mode into the system that is localized in space and oscillates with a frequency that is above the cutoff frequency of the linear monoatomic system. With the light-mass defect at the center of the lattice, we write

$$M_{m,n} = \begin{cases} M_\delta, & n = 0 \text{ and } m = 0 \\ M_b, & \text{otherwise,} \end{cases} \quad (8)$$

where $(0, 0)$ is the index of the defect magnet with mass M_δ , the quantity M_b is the mass of a magnet in the 'bulk' (i.e. the non-defect mass), and $M_\delta < M_b$. We now consider a finite lattice, for which we numerically compute the linear modes of the system with a mass defect. We use a hexagonal boundary with an edge length of $w = 6$ magnets (see figure 2(b)). One can embed this lattice into a square matrix of size $N \times N$, where $N = 2w - 1$ is the number magnets along the $n = 0$ line of the lattice. Let $X(t)$ be the $N \times N$ matrix whose (m, n) th entry is $x_{m,n}(t)$, and let $Y(t)$ be the $N \times N$ matrix whose (m, n) th entry is $y_{m,n}(t)$. We enforce the fixed hexagonal boundaries by setting the displacements of magnets with indices (m, n) such that $|m + n| > 0$. We define the $N \times N$ matrix operators L_α using the equation

$$L_\alpha Y = \alpha_1 D Y + \alpha_0 Y D + \alpha_{-1} (E^T Y E^T + E Y E - 2Y), \quad (9)$$



where $\alpha_j \in \{a_j, b_j, c_j, d_j\}$ (with $j \in \{-1, 0, 1\}$); the $N \times N$ tridiagonal matrix D has 1 entries along the super-diagonals and sub-diagonals, 2 entries along the diagonal, and 0 entries everywhere else; E is an $N \times N$ matrix with 1 entries along the super-diagonal and 0 entries everywhere else; and E^T is the transpose of E . With these definitions, equation (6) becomes

$$\begin{aligned} M \circ \ddot{X}(t) &= L_a X(t) + L_b Y(t), \\ M \circ \ddot{Y}(t) &= L_c X(t) + L_d Y(t), \end{aligned} \quad (10)$$

where M is an $N \times N$ matrix in which all entries except the $(0, 0)$ th entry (which is equal to M_δ) are equal to M_b . The operation \circ denotes pointwise multiplication (i.e. the Hadamard product). The system (10) has solutions $(X(t), Y(t))$ such that $X(t) = \tilde{X} e^{i\omega t}$ and $Y(t) = \tilde{Y} e^{i\omega t}$, where \tilde{X} and \tilde{Y} are $N \times N$ time-independent matrices and

$$-\omega^2 \begin{pmatrix} M \circ \tilde{X} \\ M \circ \tilde{Y} \end{pmatrix} = \begin{pmatrix} L_a & L_b \\ L_c & L_d \end{pmatrix} \begin{pmatrix} \tilde{X} \\ \tilde{Y} \end{pmatrix}. \quad (11)$$

One can cast equation (11) as a standard eigenvalue problem by letting $\lambda = -\omega^2$ and unwrapping the \tilde{X} and \tilde{Y} matrices into equivalent row vectors and reshaping the block matrix (with entries given by L_a) into a corresponding $2N^2 \times 2N^2$ matrix. One can then numerically solve the resulting eigenvalue problem to obtain $2N^2$ eigenvalues and their corresponding modes. Using the values in table 1 and $w = 6$ (which yields $N = 11$), we see that two eigenvalues (each with a frequency of $\sqrt{-\lambda}/(2\pi) = \omega/(2\pi) = f_d \approx 9.17$) lie above the cutoff frequency $f_c \approx 8.77$ Hz. The rotational symmetry of order 6 of the hexagonal lattice suggests that eigenvalues come in nearly resonant triplets, rather than in pairs [41]. Although this is indeed true for a homogeneous hexagonal lattice, the presence of the defect splits the largest nearly resonant triplet into a pair of eigenvalues with a frequency above the cutoff (representing the defect frequency) and a single, non-repeated eigenvalue. The spatial structures of the modes that correspond to the three largest eigenvalues confirm that there are only two defect modes. In particular, the modes that correspond to the frequency f_d have localized spatial structures (see figures 4(a) and 4(b)). By contrast, the mode that corresponds to the next-largest eigenvalue is spatially extended (see figure 4(c)).

Now suppose that there is driving and damping. Near the $(X(t), Y(t)) \equiv 0$ background state, the system (10) yields the following approximate system:

$$M \circ \ddot{X}(t) = L_a X(t) + L_b Y(t) - \gamma \dot{X}(t) + a\mathcal{A} \cos(\phi) \sin(2\pi ft), \quad (12)$$

$$M \circ \ddot{Y}(t) = L_c X(t) + L_d Y(t) - \gamma \dot{Y}(t) + a\mathcal{A} \sin(\phi) \sin(2\pi ft), \quad (13)$$

where \mathcal{A} is an $N \times N$ matrix that has all 0 entries except for the single nonzero entry

$$\mathcal{A}_{0,0} = \frac{I_0 \mu_0 \mathcal{M}}{2\pi \hbar^2}.$$

We obtain \mathcal{A} by expanding the external drive function \mathbf{F}^{ext} near the vanishing displacements and maintaining the leading, non-vanishing term. We can then find solutions of the system (12, 13) in the form

$$X(t) = \tilde{X}_1 \cos(2\pi ft) + \tilde{X}_2 \sin(2\pi ft), \quad Y(t) = \tilde{Y}_1 \cos(2\pi ft) + \tilde{Y}_2 \sin(2\pi ft), \quad (14)$$

where we obtain the $N \times N$ matrices \tilde{X}_1 , \tilde{X}_2 , \tilde{Y}_1 , and \tilde{Y}_2 by substituting equation (14) into equations (12) and (13) and then solving the resulting system of linear equations.

We use root mean square (RMS) quantities as our principal diagnostics for evaluating our results (e.g. in our numerical continuations in section 4). Unless we state otherwise, we compute the RMS of the velocity of the y -component of the center particle (i.e. $\dot{y}_{0,0}$). In this case,

$$\text{RMS} = \sqrt{\frac{\int_0^T \dot{y}_{0,0}^2(t) dt}{T}},$$

where $T = 1/f$ is the period of the excitation frequency. We show a plot of the RMS of $\dot{y}_{0,0}$ of the linear state (14) in figure 4(d) as a function of the excitation frequency for a fixed amplitude of $a = 0.01$ mV and an excitation angle of $\phi = \pi/2$. The lone resonant peak above the cutoff point is close to the estimated defect frequency $f_d \approx 9.17$ Hz.

In figure 4(e), we show a frequency sweep in our experiment for $a = 4$ mV and $\phi = \pi/2$. We show the theoretical values of the cutoff frequency $f_c \approx 8.77$ Hz and defect frequency $f_d \approx 9.17$ Hz that we found in section 3.2 as vertical solid and dashed lines, respectively. We see that the experimental resonant peak is close to the theoretical value. To obtain a cleaner resonant peak, we use an excitation amplitude that is large enough to overcome the noise in the system. One such amplitude is $a = 4$ mV. As we will see in section 4, an excitation amplitude of $a = 4$ mV is already in the nonlinear regime of the system.

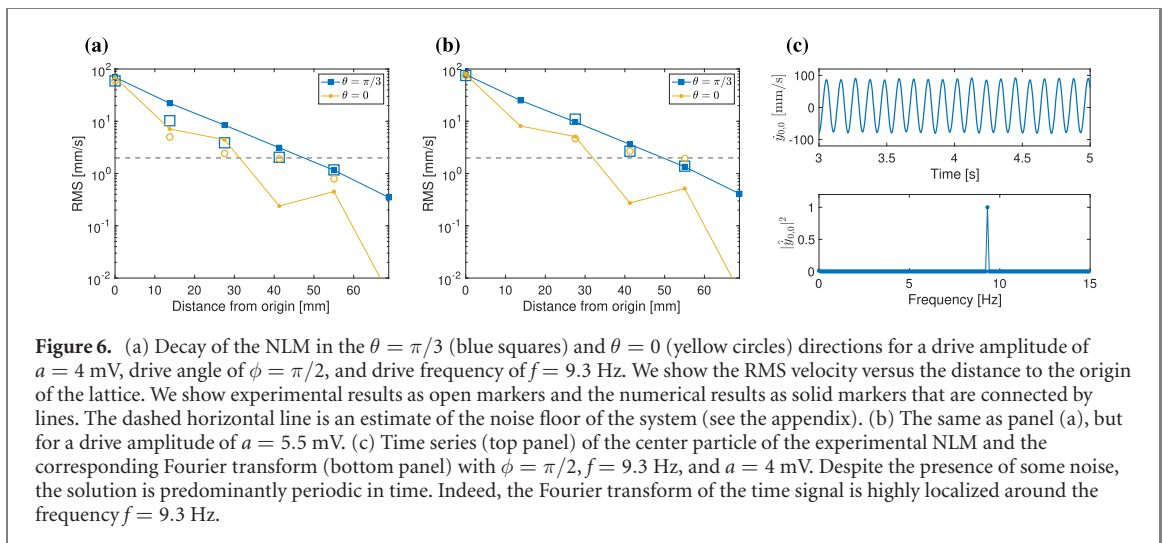
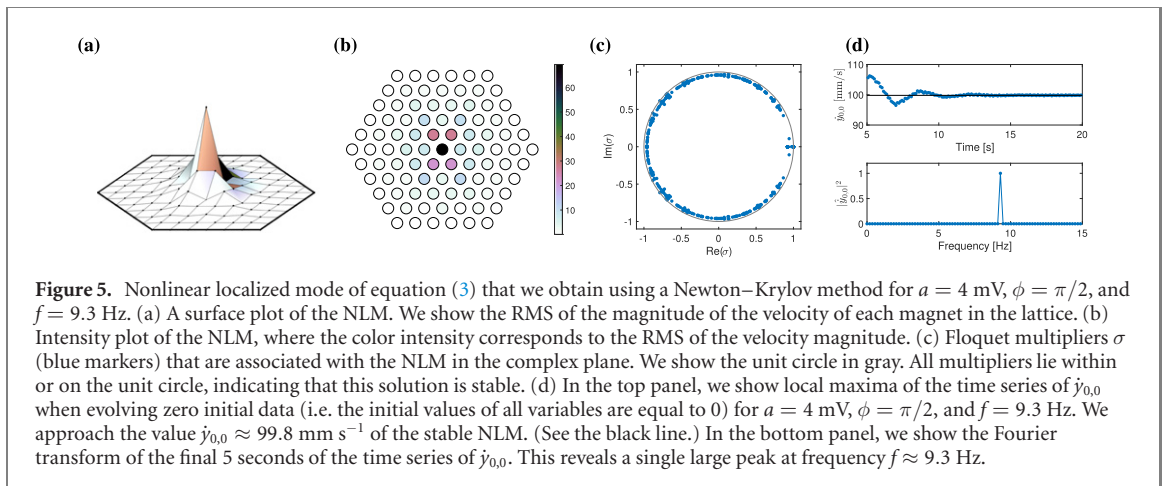
3.3. Numerical methods for the computation of nonlinear localized modes and their stability

For the remainder of our paper, we focus on how the presence of nonlinearity affects the defect-induced linear localized modes of the system (see, e.g. figure 4(d)). We refer to these solutions, which are localized in space and periodic in time, as ‘nonlinear localized modes’ (NLMs). We compute them numerically in the following manner. We compute time-periodic orbits of equation (3) with period $T = 1/f$ to high precision by finding roots of the map $G = \mathbf{x}(T) - \mathbf{x}(0)$, where $\mathbf{x}(T)$ is the solution of equation (3) at time T with initial condition $\mathbf{x}(0)$ and $\mathbf{x} \in \mathbb{R}^{4N^2}$ is the vector that results from reshaping the matrix with elements $x_{m,n}$, $y_{m,n}$, $\dot{x}_{m,n}$, and $\dot{y}_{m,n}$ into row vectors and concatenating them into a single vector. We obtain roots of the map G using a Jacobian-free Newton–Krylov method [42] with an initial guess of our linear state (14). We perform numerical continuations using a pseudo-arclength algorithm [43] with the excitation frequency f or amplitude a as our continuation parameter. We determine the linear stability of each solution \mathbf{x} by solving the variational equations $\dot{V} = (DG)V$ with the initial condition $V(0) = I$, where I denotes the identity matrix and DG is the $4N^2 \times 4N^2$ Jacobian matrix of the right-hand side of equation (3) evaluated at the solution \mathbf{x} [44]. We calculate the Floquet multipliers, which we denote hereafter by σ , for a solution by computing the eigenvalues of the matrix $V(T)$. If all of the Floquet multipliers of a solution have an absolute value that is less than or equal to 1, we say that the solution is ‘linearly stable’. Otherwise, we say that the solution is ‘unstable’. The Floquet multipliers only give information about the spectral stability of the solutions, and marginal instabilities that are associated with unit Floquet multipliers and nonlinear instabilities are possible. Therefore, we verify stability through numerical simulations. In our continuation diagrams, solid blue segments correspond to stable parameter regions and dashed red segments correspond to unstable regions. We compute the Floquet multipliers after we obtain a solution with the Newton–Krylov method to avoid repeatedly solving the large variational system. The latter computation would be necessary if we were using a standard Newton method, because the Jacobian of the map G is $V(T) - I$.

4. Main results

4.1. Numerical NLMs

Using the Newton–Krylov method that we described in section 3.3, we obtain a time-periodic solution with $f = 9.3$ Hz, $a = 4$ mV, and $\phi = \pi/2$. Additionally, because $f = 9.3 > 8.77 \approx f_c$, this solution is localized in space (see figure 5(a)). The dominant peak is at the center of the lattice, and the magnets that are adjacent



to the center magnet at angles $\pi/3$, $2\pi/3$, $4\pi/3$, and $5\pi/3$ have the next-largest amplitudes (see figure 5(b)). This is not surprising because we are exciting the lattice along the $\phi = \pi/2$ direction. The Floquet multipliers that are associated with this solution each have a magnitude that is no larger than 1, indicating that the solution is stable (see figure 5(c)). Indeed, upon simulating equation (3) with the initial values of all variables equal to 0 (i.e. ‘zero initial data’) and $f = 9.3$ Hz, $a = 4$ mV, and $\phi = \pi/2$, the dynamics approaches this stable NLM. (See the top panel of figure 5(d).) As expected, the Fourier transform of the corresponding time series is localized around the frequency $f \approx 9.3$ Hz.

The spatial decay of the tails of the NLM depends on which direction of observation one considers. For example, if one measures the RMS velocity of the magnets that lie along the $\theta = \pi/3$ direction, the decay appears to be exponential or faster. See the solid blue squares in figure 6(a), which shows the RMS velocity versus distance from the origin (following the $\theta = \pi/3$ direction) in a semilogarithmic plot for the NLM from figure 5 (i.e. for the NLM with $f = 9.3$ Hz, $a = 4$ mV, and $\phi = \pi/2$). This is consistent with the spatial decay properties of breathers and standing waves in continuous-space settings, such as the one in [45]. The tails of the breathers therein decay at the rate e^{-br}/\sqrt{r} , where $b > 0$ is a constant. The solid yellow circles in figure 6(a) illustrate a similar decay for the magnets along the $\theta = 0$ direction for our NLM solution, although we observe some modulation in the decay profile, in contrast to the dynamics when $\theta = \pi/3$. (Modulations in spatial decay have been studied in other settings, such as in the biharmonic ϕ^4 model [46].) We observe similar decay properties for an NLM with $f = 9.3$ Hz, $a = 5.5$ mV and $\phi = \pi/2$ (see figure 6(b)).

4.2. Experimental NLMs

In our experiments, it is difficult to initialize the system with predetermined positions and velocities. To obtain an NLM, we excite the system with a small amplitude ($a = 1$ mV), which we increase gradually to the value $a = 4$ mV over about 3 min. Because we predict that there is a stable NLM at the resulting parameter values, we record data for a sufficiently long time (specifically, after 90 periods of motion have

elapsed) once we attain the value $a = 4$ mV. We track the velocities at the center particle with a laser vibrometer (see section 2), and we record the time series of the magnet velocities using an oscilloscope. (See the top panel of figure 6(c).) As expected, we obtain dynamics that are periodic in time, as we can see not only in the time series but also via its Fourier transform (which we show in the bottom panel of figure 6(c)). We obtain similar experimental results for an amplitude of $a = 5.5$ mV.

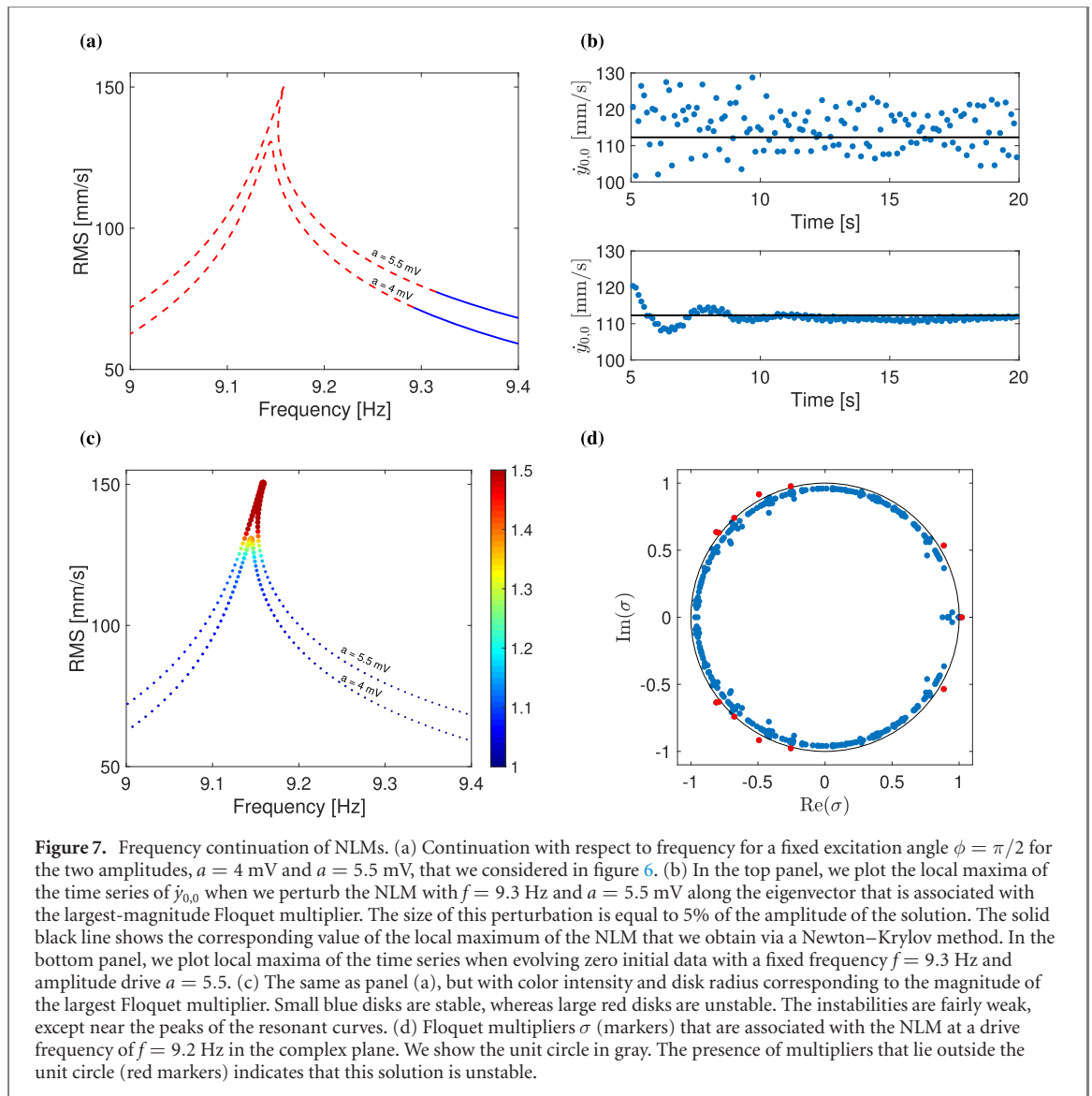
To examine the spatial decay of the experimental NLM, we record the positions of the magnets in half of the lattice using a digital camera (see section 2). By numerically differentiating the positions, we obtain an estimate for the velocities of these magnets. We were unable to measure all magnets because the DIC software loses track of some of them (if, e.g. the magnets begin to spin). However, we captured enough data to compute the decay along the two primary directions ($\theta = \pi/3$ and $\theta = 0$) that we examined in our numerical NLMs. For data that we obtained with $f = 9.3$ Hz, $a = 4$ mV, and $\phi = \pi/2$, the open blue squares in figure 6(a) show the decay along the $\theta = \pi/3$ direction and the open yellow circles show the decay along the $\theta = 0$ direction. The horizontal dashed line is our estimated mean value of the noise (see section 2). We show the experimental decay rates along with our numerical results. Although the numerical values overestimate the RMS velocity, the agreement is still reasonable, especially for the center magnet. We find similar decay properties in our experiment with $f = 9.3$ Hz, $a = 5.5$ mV, and $\phi = \pi/2$. (See the open markers of figure 6(b).)

Recall that we do not tune the numerical results to fit the experimentally obtained NLM solution. Instead, we determine each of the parameter values beforehand, as described in section 2.

4.3. Frequency continuation

In figures 4(e), 6(a), and 6(b), we demonstrated that our model (3) agrees reasonably well with our experimental data. We now conduct a series of numerical computations in the form of parameter continuation (see section 3.3 for a description of our procedure) to get a better sense of the role of the nonlinearity in equation (3) and its interplay with the disorder (at the center magnet) and the discreteness of the model. We return to our experiments in section 4.4 to see what nonlinear effects we are able to capture in the laboratory.

We first perform continuation with respect to the excitation frequency f for a fixed excitation angle $\phi = \pi/2$ for various values of the excitation amplitude a . We thereby generate nonlinear analogs of the linear resonant peak that we showed in figure 4(d). In figure 7(a), we show frequency continuations for our two drive amplitudes, $a = 4$ mV and $a = 5.5$, of the NLMs from figures 5, 6(a), and 6(b). By comparing these frequency continuations to the linear case in figure 4(d), we see that the nonlinearity deforms the peak, which becomes narrower and starts to bend toward higher frequencies. The nonlinearity also destabilizes the solutions at some critical frequency; this occurs at $f \approx 9.29$ Hz for $a = 4$ mV and at $f \approx 9.31$ Hz for $a = 5.5$ mV. Therefore, the NLM in figure 6(c) is unstable. Our numerical computations predicted this NLM to be unstable, so it is notable that we are able to access it in our experiments. Although this seems to imply that our theory is inconsistent with our experiments for the parameter values $f \approx 9.31$ Hz and $a = 5.5$ mV, the instability of the NLM for these parameter values is rather weak (with $\max(|\sigma_i|) \approx 1.007$). We observe instability only after many periods when we perturb the NLM along the eigenvector that is associated with the unstable Floquet multiplier $\sigma \approx 1.007$. See the top panel of figure 7(b). However, if we initialize the dynamics with zero initial data, we approach and stay close to the NLM solution that we obtained via a Newton–Krylov method, even after 200 periods of motion. See the bottom panel of figure 7(b). This suggests that solutions with weak instabilities can still attract nearby points in phase space, at least initially, and that our numerical prediction for $f \approx 9.31$ Hz and $a = 5.5$ mV is consistent with our experimental observations. Figure 7(c) is the same as figure 7(a), but now the color scale corresponds to the magnitude of the maximum Floquet multiplier. This illustrates that the magnitude of the instability is weak throughout most of the solution branch. The instability has its largest growth rate (with $\max(|\sigma_i|) \approx 2.15$) at the peak of the resonant curve. The instability of the NLM with $a = 5.5$ mV arises from a pair of complex-conjugate Floquet multipliers that depart from the unit circle at approximately $f = 9.31$ Hz. As the frequency decreases, additional multipliers depart from the unit circle. In figure 7(d), we show the Floquet spectrum for $f = 9.2$ Hz, indicating that there are purely real multipliers (corresponding to exponential growth) and complex multipliers (corresponding to oscillatory instabilities). Although we show only the principal branches of the NLMs in figure 7(a), it is possible that other bifurcations also occur. Indeed, the non-real nature of the Floquet multipliers that depart from the unit circle suggest that there may be other types of solutions, such as quasiperiodic ones. We investigate this possibility in section 4.4. At smaller drive frequencies (within the pass band), the solutions on the main branch of NLMs can be stable. We do not investigate such solutions in depth, however, because they are spatially extended (and hence outside the scope of the present paper).



In figure 8(a), we show the gradual bending of the resonant peak for progressively larger excitation amplitudes for the excitation angle $\phi = \pi/2$. In particular, for $a = 15$ mV, the peak bends so far that additional solutions emerge at $f \approx 9.3$ Hz. However, these large-amplitude solutions are very unstable, and we were not able to access them either in our direct numerical simulations or in our experiments. Indeed, as we will discuss in section 4.4, we observe different types of dynamics at large excitation amplitudes. We can also tune the excitation angle ϕ and thereby deform the resonant peak in a different way. For example, when we fix the excitation angle to $\phi = 0$ (i.e. an excitation along $n = 0$), the resonant curves are qualitatively similar to those for $\phi = \pi/2$ for excitation amplitudes of $a = 1$, $a = 2$, and $a = 4$ (see figure 8(b)), although the stability properties are slightly different. For the large excitation of $a = 15$ mV, the resonant curve bends even farther toward higher frequencies. Even greater qualitative differences occur for $\phi = \pi/3$ (i.e. an excitation along $m = 0$); see figure 8(c). In this case, for small-amplitude excitations, the resonant peak has a unimodal shape, as expected. However, as we consider gradually larger excitation amplitudes, an additional peak begins to emerge from the main solution branch, leading to a two-humped profile in the dependence of the RMS velocity on the frequency. This deformation is noticeable for relatively small excitation amplitudes. Specifically, we observe the existence of multiple solutions even for excitation amplitudes that are as small as $a = 3$ mV, for which there is bifurcation at frequency $f \approx 9.28$ Hz.

The frequency continuation with the excitation angle $\phi = \pi/3$ is more representative of ‘typical’ angles than the special cases $\phi = \pi/2$ and $\phi = 0$. For example, even by decreasing the angle slightly from $\phi = \pi/2$ to $\phi = 89\pi/180$, we observe the additional branch in the frequency continuation (see figure 9(a)). We show an intensity plot of the RMS velocity magnitudes of an NLM at frequency $f = 9.2$ Hz that belongs to the main branch (i.e. the branch with smaller-amplitude NLMs) of the $\phi = 89\pi/180$ continuation in figure 9(b). It has a similar profile to the NLM in figure 5. We show an intensity plot of the RMS velocity

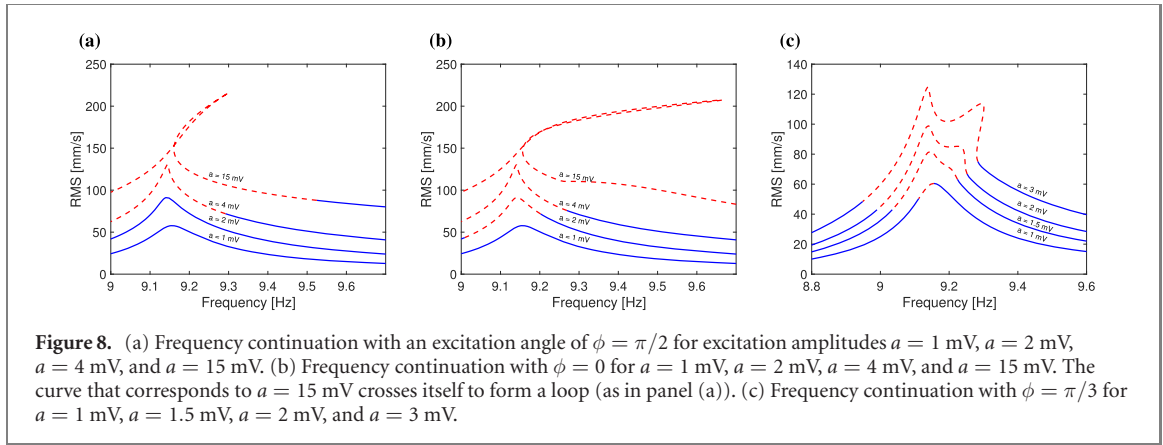


Figure 8. (a) Frequency continuation with an excitation angle of $\phi = \pi/2$ for excitation amplitudes $a = 1$ mV, $a = 2$ mV, $a = 4$ mV, and $a = 15$ mV. (b) Frequency continuation with $\phi = 0$ for $a = 1$ mV, $a = 2$ mV, $a = 4$ mV, and $a = 15$ mV. The curve that corresponds to $a = 15$ mV crosses itself to form a loop (as in panel (a)). (c) Frequency continuation with $\phi = \pi/3$ for $a = 1$ mV, $a = 1.5$ mV, $a = 2$ mV, and $a = 3$ mV.

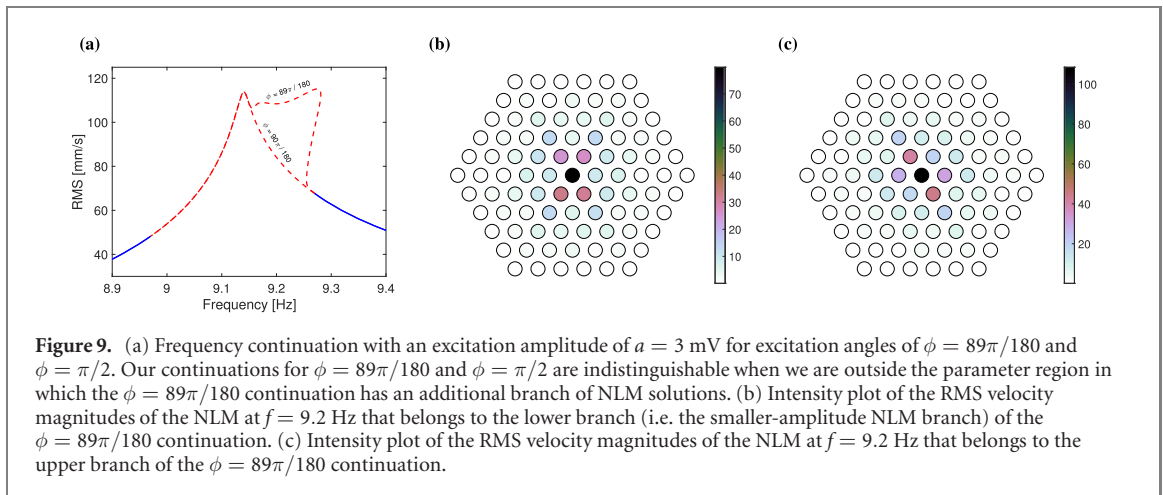


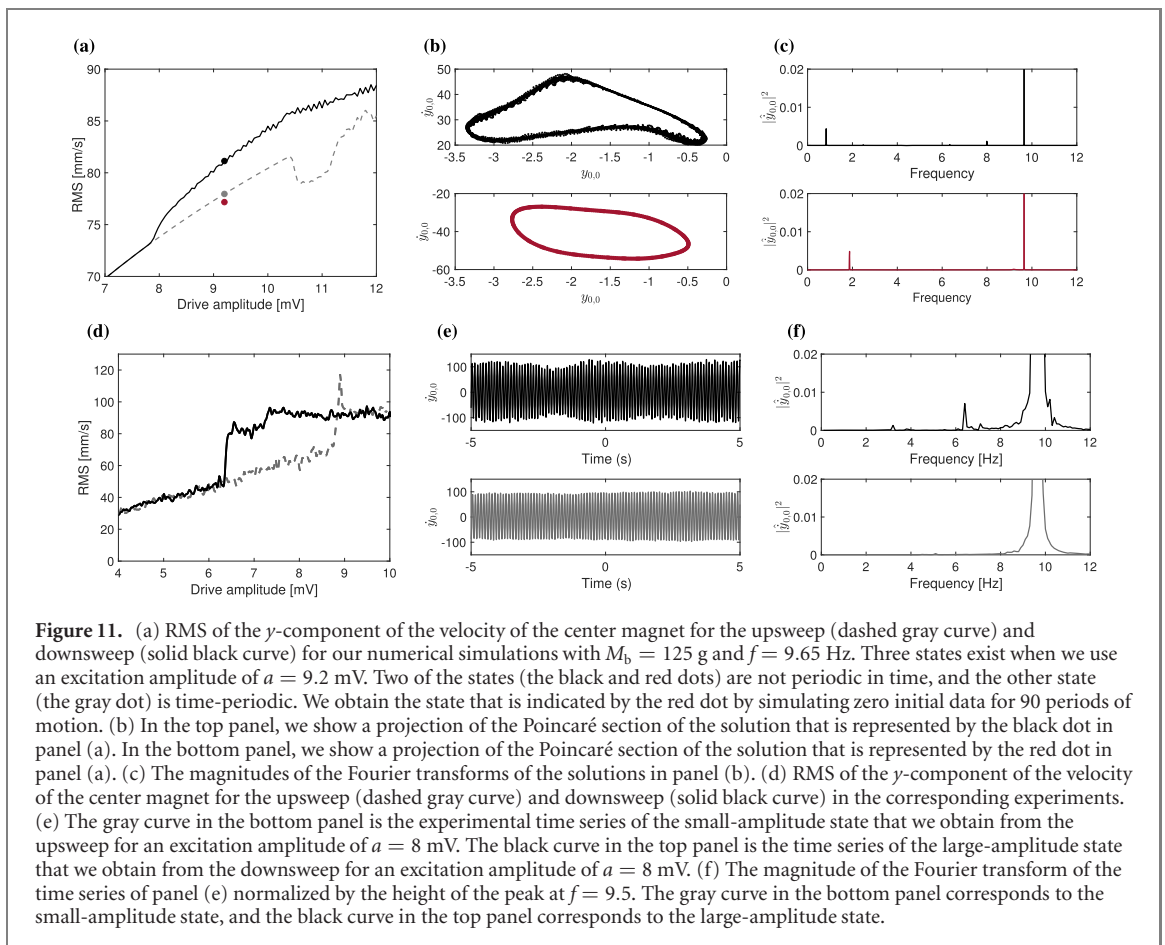
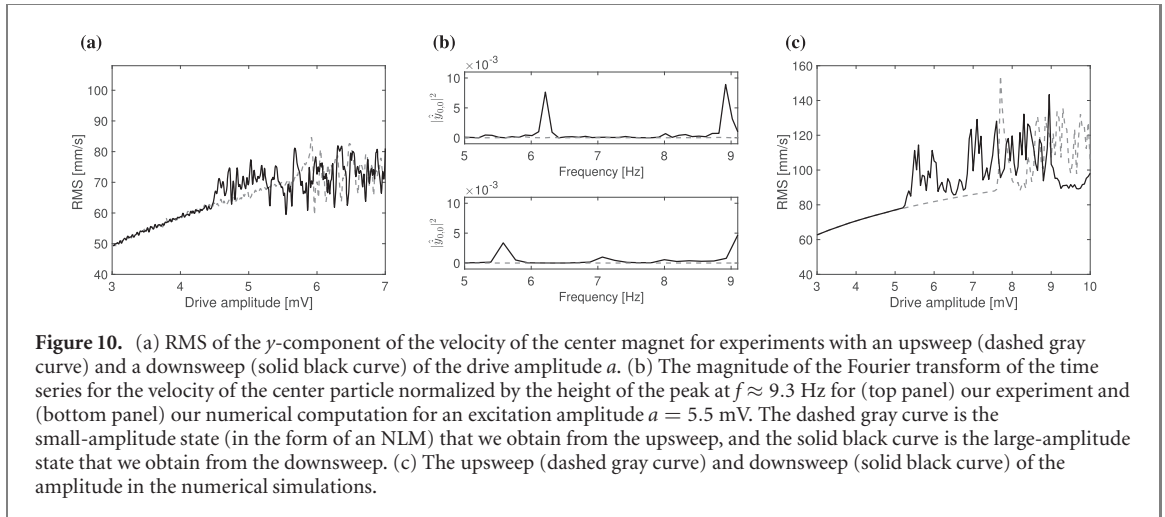
Figure 9. (a) Frequency continuation with an excitation amplitude of $a = 3$ mV for excitation angles of $\phi = 89\pi/180$ and $\phi = \pi/2$. Our continuations for $\phi = 89\pi/180$ and $\phi = \pi/2$ are indistinguishable when we are outside the parameter region in which the $\phi = 89\pi/180$ continuation has an additional branch of NLM solutions. (b) Intensity plot of the RMS velocity magnitudes of the NLM at $f = 9.2$ Hz that belongs to the lower branch (i.e. the smaller-amplitude NLM branch) of the $\phi = 89\pi/180$ continuation. (c) Intensity plot of the RMS velocity magnitudes of the NLM at $f = 9.2$ Hz that belongs to the upper branch of the $\phi = 89\pi/180$ continuation.

magnitudes of an NLM from the other (i.e. larger-amplitude) branch at $f = 9.2$ Hz in figure 9(c). The solutions along this branch have secondary amplitudes in the $-\pi/3$ direction. It appears that the asymmetric nature of the drive is responsible for the excitation of this additional solution, whose profile is distinct from the solutions in the main branch.

4.4. Drive-amplitude sweeps

We now return to the effect of large-amplitude excitations for the parameter set—namely, $\phi = \pi/2$ and $f \approx 9.3$ Hz—in our laboratory experiments. Our bifurcation analysis revealed that the NLM solution at this parameter set destabilizes for larger amplitudes, although sometimes the instability is so weak that the NLMs are effectively stable on short enough time scales (see figure 7(b)). For the parameter values $\phi = \pi/2$ and $f \approx 9.3$ Hz, we also observed that a large-amplitude branch of NLM solutions emerges for sufficiently large excitation amplitudes (see figure 8(a)).

To study the dynamics at larger amplitudes in experiments, we initialize the system with a small-amplitude excitation (of $a = 1$ mV) and gradually increase the amplitude in increments of 0.05 mV. For each step, we run the system for 90 periods, which allows sufficient time to settle to a steady state if there is one. We record the RMS of the velocity of the center magnet for the final 5 seconds. We call this procedure an amplitude ‘upsweep’. We use an analogous procedure when we start with a large excitation amplitude, which we gradually decrease in steps of size 0.05 mV. We call this procedure an amplitude ‘downsweep’. We show our experimental results for both an upsweep and a downsweep in figure 10(a). For sufficiently small amplitudes (specifically, for $a \lesssim 4.5$ mV), the upsweep and downsweep approach the same NLM, suggesting that there is a single stable branch of NLMs for $a \lesssim 4.5$ mV. However, for $a \gtrsim 4.5$ mV, there appear to be two different states; we obtain the small-amplitude states when we perform an upsweep and the large-amplitude states when we perform a downsweep. The small-amplitude states have the form of an NLM. The experimental result in figure 6(b) is an example of the small-amplitude state for $a = 5.5$ mV. The large-amplitude states are also localized, but they are no longer periodic in time. An inspection of the Fourier transform of the large-amplitude state for $a = 5.5$ mV reveals other peaks in the spectrum (in addition to a peak at the excitation frequency $f \approx 9.3$ Hz). In the top panel of figure 10(b), we show the



Fourier transform of both the large-amplitude state and the small-amplitude state. The small-amplitude state (i.e. the NLM) has no peaks for lower frequencies, whereas the large-amplitude state has peaks at approximately $f = 8.9$ Hz and $f = 6.2$ Hz; this is suggestive of quasiperiodic behavior.

We obtain qualitatively similar results when we perform analogous upsweeps and downsweeps in numerical computations. We also observe the emergence of two states in these computations (see figure 10(c)). In our computations, the large-amplitude state departs from the branch of NLMs for excitation amplitudes that are slightly larger (specifically, for $a \gtrsim 5.1$ mV) than the ones in our experiments. The amplitude $a \approx 5.1$ mV is roughly where the numerical NLM branch destabilizes. As in our experiments, these large-amplitude states are not periodic in time. One can also observe the presence of secondary peaks in their Fourier transforms in our numerical solutions, although the locations of these peaks are slightly different than in our experiments. See the bottom panel of figure 10(b). Although these numerical large-amplitude states have features that are similar to those of time-quasiperiodic states (given

the multiple incommensurate peaks in the Fourier transform), it is also possible that these large-amplitude states are weakly chaotic. One issue is that we were unable to detect asymptotically stable time-quasiperiodic orbits for parameter values that correspond to those in the experiments. If these solutions were attractors, it would be straightforward to determine if the large-amplitude states are time-quasiperiodic ones by plotting Poincaré sections of the orbits.

To clarify the nature of the large-amplitude states, we modify the parameter values slightly to obtain stable time-quasiperiodic solutions. We perform amplitude upsweeps and downsweeps for the parameter set $\phi = \pi/2$, $f = 9.65$ Hz, and $M_b = 125$ g. We use a different drive frequency from our prior calculations because the smaller mass $M_b = 125$ g leads to a cutoff frequency of $f_c \approx 9.01$ Hz and a defect frequency of $f_d \approx 9.36$ Hz. The amplitude sweeps with these parameter values lead to a well-defined large-amplitude branch of solutions that bifurcates from the main branch of periodic solutions (the NLMs) (see figure 11(a)). In figure 11(a), we show three solid markers to point out the locations of three solutions: a large-amplitude state that appears to be either time-quasiperiodic or time-chaotic in black, the NLM (in gray), and a stable time-quasiperiodic orbit (in red). We show a plot of a projection of the Poincaré section in the $(y_{0,0}, \dot{y}_{0,0})$ plane in figure 11(b) for the two states that are not time-periodic. The orbit in the bottom panel reveals a well-defined invariant curve, illustrating the quasiperiodic nature of the solution. We show the Fourier transforms of these two non-periodic states in figure 11(c). Both have a secondary peak in their spectrum, demonstrating that the solutions are indeed non-periodic in time (because of the incommensurate peaks in the frequency spectra). Laboratory experiments for this modified parameter set yield similar results. In particular, there is a well-defined large-amplitude branch of solutions that bifurcates from a branch of time-periodic solutions (see figures 11(d) and 11(e)). The Fourier transform of one of the large-amplitude states also has a secondary peak in the spectrum, an indication that the state is nearly quasiperiodic. For simplicity, we henceforth use the term ‘quasiperiodic’ for such a state.

Because our numerical computations and experiments with bulk magnets of mass $M_b = 125$ g reveal the existence of time-quasiperiodic orbits that bifurcate from the main branch of time-periodic NLMs, it is reasonable to conclude that these quasiperiodic solutions persist when we continue the parameters to the original parameter set $M_b = 138.2$ g and $f_d = 9.3$. This suggests that the large-amplitude branch in figures 10(a) and 10(c) consists of time-quasiperiodic solutions.

5. Conclusions

We have demonstrated, both experimentally and numerically, the existence of NLMs in a 2D hexagonal lattice of repelling magnets. By exploring the effects of nonlinearity numerically using frequency continuation and experimentally using amplitude sweeps, we revealed the emergence of both time-periodic NLMs and time-quasiperiodic localized states. We have also established that our experimental setup is a viable approach for fundamental studies in nonlinear lattice systems that go beyond what is possible in 1D chains. We found that the smaller-amplitude NLMs that we considered are stable, whereas progressively larger excitation amplitudes lead to instabilities and more complicated dynamics, including time-quasiperiodic and potentially time-chaotic behavior. We also explored the anisotropy of the hexagonal lattice by considering different excitation angles and examining the nature and decay of the states along these angles.

Our work paves the way for many future studies. For example, although our parameter continuation in frequency revealed several families of solutions, there are undoubtedly—given the complexity of the studied system—several other ones (possibly including exotic ones) to discover. Other avenues of future work include the study of refined models—such as ones that account for nonlinear damping (or, more generally, a more elaborate form of damping [47–49]), rotational effects (which can be rather important [50, 51]), and/or long-range interactions [38]—of our lattice system. Each of these aspects will add elements of complexity, but they also may lead to other types of interesting dynamics, such as the possibility of breather solutions with algebraically decaying tails in space [38, 39]. It is also possible that the inclusion of rotational effects and/or more sophisticated damping models may help improve matches with laboratory experiments. Such models have an associated cost of being more complicated and hence more cumbersome to analyze and simulate. Our attempt in the present paper has been to explore the principal features of the interplay of discreteness, local disorder, and nonlinearity in a hexagonal lattice of magnets. Breathers in heterogeneous hexagonal magnetic lattices (e.g. ones with a repeating pattern of two masses) may lead to the existence of ILMs and are also worthy of future study. Accordingly, investigations of band gaps, instabilities, and nonlinear modes and their propagation are topics of substantial ongoing interest.

Data-availability statement

The data that support the findings of this study are available upon reasonable request from the authors.

Acknowledgments

The present paper is based on work that was supported by the US National Science Foundation under Grant Nos. DMS-1615037 (CC), DMS-1809074 (PGK), and EFRI-1741565 (CD). AJM acknowledges support from the Agencia Nacional de Investigación y Desarrollo de Chile (ANID) under Grant No. 3190906. EGC thanks Bowdoin College, where the initial stages of this work were carried out, for their kind hospitality. PGK also acknowledges support from the Leverhulme Trust via a Visiting Fellowship and thanks the Mathematical Institute of the University of Oxford for its hospitality during part of this work. We give special thanks to Bowdoin undergraduates Ariel Gonzales, Patrycja Pekala, Anam Shah, and Steven Xu for help with simulations and data management.

Appendix.

Derivation of the external force from the wire: To derive the external force that the wire exerts on a magnet, we first define our coordinate system. We choose orthogonal unit vectors \hat{r} , \hat{z} , and \hat{s} that are centered on the wire and oriented such that the wire is aligned with the \hat{s} axis (see figure 12(a)). We model the magnetic moment \mathcal{M} of the magnet using the Gilbert model of a magnetic dipole [52]:

$$\mathbf{F}_{\text{wire}} = \nabla (\mathcal{M} \cdot \mathbf{B}), \quad (15)$$

which describes the force that acts on the dipole due to the magnetic field \mathbf{B} . In our setup, the wire carries an electric current I that generates the magnetic field $\mathbf{B}(r, z) = B_r(r, z)\hat{r} + B_z(r, z)\hat{z}$. Evaluating \mathbf{B} at the position $-h\hat{z} + r\hat{r}$ of the magnet yields

$$\mathbf{B}(r, -h) = \frac{I\mu_0}{2\pi\sqrt{h^2 + r^2}} (\sin \theta \hat{r} + \cos \theta \hat{z}), \quad (16)$$

where μ_0 is the magnetic permeability and θ is the angle between \mathbf{B} and \mathcal{M} . We assume that we can neglect the dynamics along the \hat{z} axis, so we are interested only in the \hat{r} component of the force. Inserting equation (16) into equation (15) and taking $\mathcal{M} = \mathcal{M}\hat{z}$, we obtain

$$\mathbf{F}_{\text{wire}} = \mathcal{M} \partial_r B_z(r, z) \hat{r} = \frac{I\mu_0\mathcal{M}}{2\pi} \frac{h^2 - r^2}{(h^2 + r^2)^2} \hat{r}, \quad (17)$$

which corresponds to equation (1). In our coordinates, the wire is orthogonal to the plane that is spanned by the lattice basis vectors $\mathbf{e}_1 = (1, 0)$ and $\mathbf{e}_2 = (1/2, \sqrt{3}/2)$. It is straightforward to write equation (17) in coordinates in the $\{\mathbf{e}_1, \mathbf{e}_2\}$ basis by including a parameter ϕ that accounts for the excitation angle. For instance, for the center magnet, we may write

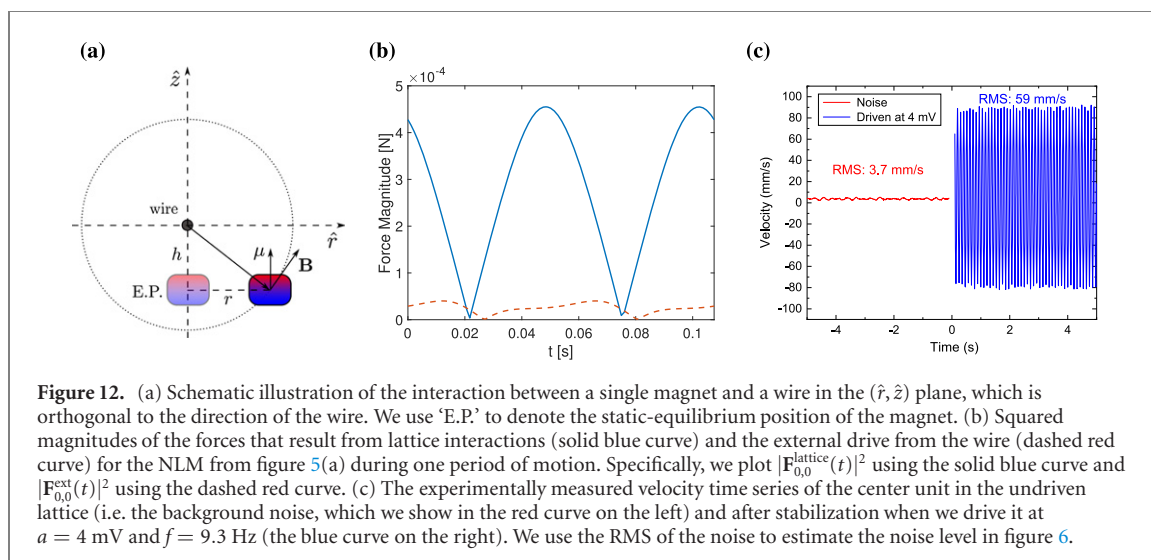
$$\mathbf{F}_{0,0}^{\text{ext}} = \frac{I\mu_0\mathcal{M}}{2\pi} \begin{pmatrix} \cos(\phi) \frac{h^2 - x_{0,0}^2}{(h^2 + x_{0,0}^2)^2} \\ \sin(\phi) \frac{h^2 - y_{0,0}^2}{(h^2 + y_{0,0}^2)^2} \end{pmatrix}, \quad (18)$$

which corresponds to equation (4).

Comparison of external and internal nonlinear forces: Although the form of the force of the external drive is specific to our experimental setup, the dynamics are dominated by the lattice forces. For example, in figure 12(b), we compare the forces that result from the wire (see equation (18)) and the force from the lattice for the NLM of figure 5(a). The lattice forces are

$$\begin{aligned} \mathbf{F}_{m,n}^{\text{lattice}} = & -\mathbf{F}_0(\mathbf{q}_{m+1,n} - \mathbf{q}_{m,n}) - \mathbf{F}_1(\mathbf{q}_{m,n+1} - \mathbf{q}_{m,n}) + \mathbf{F}_{-1}(\mathbf{q}_{m,n} - \mathbf{q}_{m-1,n+1}) \\ & + \mathbf{F}_0(\mathbf{q}_{m,n} - \mathbf{q}_{m-1,n}) + \mathbf{F}_1(\mathbf{q}_{m,n} - \mathbf{q}_{m,n-1}) - \mathbf{F}_{-1}(\mathbf{q}_{m+1,n-1} - \mathbf{q}_{m,n}). \end{aligned} \quad (19)$$

However, it is important to acknowledge that the effective ‘defect’ that is produced by the force (19) is responsible for the presence of the corresponding linear defect frequency and hence for the associated NLMs in the presence of nonlinearity.



Noise estimation: Even if we do not apply an external drive to the lattice, the particles still exhibit detectable motion. This is due to interactions with the air flow from the table and to imperfections (e.g. nonaxisymmetric mass distributions) of the particles. To estimate the noise floor of the system, we measure the velocity time series of the center particle when there is no drive. The corresponding RMS velocity is our noise estimate. We find that the RMS velocity of the noise is 6% of the RMS velocity of the system when we drive it at 4 mV (see figure 12(c)).

ORCID iDs

Christopher Chong <https://orcid.org/0000-0002-4908-3252>

Yifan Wang <https://orcid.org/0000-0003-2284-520X>

Efstathios G Charalampidis <https://orcid.org/0000-0002-5417-4431>

Mason A Porter <https://orcid.org/0000-0002-5166-0717>

Panayotis G Kevrekidis <https://orcid.org/0000-0002-7714-3689>

References

- [1] Lederer F, Stegeman G I, Christodoulides D N, Assanto G, Segev M and Silberberg Y 2008 Discrete solitons in optics *Phys. Rep.* **463** 1
- [2] Binder P, Abraimov D, Ustinov A V, Flach S and Zolotaryuk Y 2000 Observation of breathers in Josephson ladders *Phys. Rev. Lett.* **84** 745
- [3] Trías E, Mazo J J and Orlando T P 2000 Discrete breathers in nonlinear lattices: experimental detection in a Josephson array *Phys. Rev. Lett.* **84** 741
- [4] English L Q, Sato M and Sievers A J 2003 Modulational instability of nonlinear spin waves in easy-axis antiferromagnetic chains. II. Influence of sample shape on intrinsic localized modes and dynamic spin defects *Phys. Rev. B* **67** 024403
- [5] Schwarz U T, English L Q and Sievers A J 1999 Experimental generation and observation of intrinsic localized spin wave modes in an antiferromagnet *Phys. Rev. Lett.* **83** 223
- [6] Swanson B I, Brozik J A, Love S P, Strouse G F, Shreve A P, Bishop A R, Wang W-Z and Salkola M I 1999 Observation of intrinsically localized modes in a discrete low-dimensional material *Phys. Rev. Lett.* **82** 3288
- [7] Peyrard M 2004 Nonlinear dynamics and statistical physics of DNA *Nonlinearity* **17** R1
- [8] Bajars J, Eilbeck J C and Leimkuhler B 2015 *Numerical Simulations of Nonlinear Modes in Mica: Past, Present and Future* (Berlin: Springer) p 35
- [9] Morsch O and Oberthaler M 2006 Dynamics of Bose–Einstein condensates in optical lattices *Rev. Mod. Phys.* **78** 179
- [10] Flach S and Gorbach A 2008 Discrete breathers: advances in theory and applications *Phys. Rep.* **467** 1
- [11] Kevrekidis P G 2011 Non-linear waves in lattices: past, present, future *IMA J. Appl. Math.* **76** 389
- [12] Dmitriev S V, Korznikova E A, Baimova Y A and Velarde M G 2016 Discrete breathers in crystals *Phys.-Usp.* **59** 446
- [13] Fermi E, Pasta J and Ulam S 1955 Studies of nonlinear problems. I *Tech. Rep.* Los Alamos, NM, USA: Los Alamos National Laboratory LA-1940
- [14] Gallavotti G 2008 *The Fermi–Pasta–Ulam Problem: A Status Report* (Heidelberg: Springer)
- [15] Nesterenko V F 2001 *Dynamics of Heterogeneous Materials* (Heidelberg: Springer)
- [16] Chong C and Kevrekidis P G 2018 *Coherent Structures in Granular Crystals: From Experiment and Modelling to Computation and Mathematical Analysis* (Heidelberg: Springer)
- [17] Starosvetsky Y, Jayaprakash K R, Hasan M A and Vakakis A F 2017 *Topics on the Nonlinear Dynamics and Acoustics of Ordered Granular Media* (Singapore: World Scientific)
- [18] Chong C, Porter M A, Kevrekidis P G and Daraio C 2017 Nonlinear coherent structures in granular crystals *J. Phys.: Condens. Matter* **29** 413003

- [19] Molerón M, Leonard A and Daraio C 2014 Solitary waves in a chain of repelling magnets *J. Appl. Phys.* **115** 184901
- [20] Mehrem A, Jiménez N, Salmerón-Contreras L J, García-Andrés X, García-Raffi L M, Picó R and Sánchez-Morcillo V J 2017 Nonlinear dispersive waves in repulsive lattices *Phys. Rev. E* **96** 012208
- [21] Serra-García M, Molerón M and Daraio C 2018 Tunable, synchronized frequency down-conversion in magnetic lattices with defects *Phil. Trans. R. Soc. A.* **376** 20170137
- [22] Marin J L, Eilbeck J C and Russell F M 1998 Localized moving breathers in a 2D hexagonal lattice *Phys. Lett. A* **248** 225
- [23] Marin J L, Eilbeck J C and Russell F M 2000 *2-D Breathers and Applications* vol 542 (Heidelberg: Springer) p 293
- [24] English L Q, Palmero F, Stormes J F, Cuevas J, Carretero-González R and Kevrekidis P G 2013 Nonlinear localized modes in two-dimensional electrical lattices *Phys. Rev. E* **88** 022912
- [25] Vladimirov S V and Ostrikov K 2004 Dynamic self-organization phenomena in complex ionized gas systems: new paradigms and technological aspects *Phys. Rep.* **393** 175
- [26] Koukoulouyannis V, Kevrekidis P G, Law K J H, Kourakis I and Frantzeskakis D J 2010 Existence and stability of multisite breathers in honeycomb and hexagonal lattices *J. Phys. A: Math. Theor.* **43** 235101
- [27] Wattis J A D 2015 *Asymptotic Approximation of Discrete Breather Modes in Two-Dimensional Lattices* vol 221 (Heidelberg: Springer) p 179
- [28] Flach S, Kladko K and Takeno S 1997 Acoustic breathers in two-dimensional lattices *Phys. Rev. Lett.* **79** 4838
- [29] Lü B-B and Qiang T 2009 Discrete gap breathers in a two-dimensional diatomic face-centered square lattice *Chin. Phys. B* **18** 4393
- [30] Koukoulouyannis V and Kourakis I 2009 Discrete breathers in hexagonal dusty plasma lattices *Phys. Rev. E* **80** 026402
- [31] Feng B-F and Kawahara T 2007 Discrete breathers in two-dimensional nonlinear lattices *Wave Motion* **45** 68
- [32] Maradudin A A, Montroll E W and Weiss G H 1963 *Theory of Lattice Dynamics in the Harmonic Approximation* (New York: Academic)
- [33] Theocharis G, Kavousanakis M, Kevrekidis P G, Daraio C, Porter M A and Kevrekidis I G 2009 Localized breathing modes in granular crystals with defects *Phys. Rev. E* **80** 066601
- [34] Bowcock P, Corrigan E and Zambon C 2005 Some aspects of jump-defects in the quantum sine-gordon model *J. High Energy Phys.* **JHEP08(2005)023**
- [35] Boechler N, Theocharis G and Daraio C 2011 Bifurcation-based acoustic switching and rectification *Nat. Mater.* **10** 665
- [36] Hoogeboom C, Man Y, Boechler N, Theocharis G, Kevrekidis P G, Kevrekidis I G and Daraio C 2013 Hysteresis loops and multi-stability: from periodic orbits to chaotic dynamics (and back) in diatomic granular crystals *Europhys. Lett.* **101** 44003
- [37] Chong C, Foehr A, Charalampidis E G, Kevrekidis P G and Daraio C 2019 Breathers and other time-periodic solutions in an array of cantilevers decorated with magnets *Math. Eng.* **1** 489
- [38] Molerón M, Chong C, Martínez A J, Porter M A, Kevrekidis P G and Daraio C 2019 Nonlinear excitations in magnetic lattices with long-range interactions *New J. Phys.* **21** 063032
- [39] Flach S 1998 Breathers on lattices with long range interaction *Phys. Rev. E* **58** R4116
- [40] Steidel R F 1989 *An Introduction to Mechanical Vibrations* (New York: Wiley)
- [41] Lepidi M 2013 Multi-parameter perturbation methods for the eigensolution sensitivity analysis of nearly-resonant non-defective multi-degree-of-freedom systems *J. Sound Vib.* **332** 1011
- [42] Kelley C T 2003 *Solving Nonlinear Equations with Newton's Method* (Philadelphia, PA: Society for Industrial and Applied Mathematics)
- [43] Doedel E and Tuckerman L S 2000 *Numerical Methods for Bifurcation Problems and Large-Scale Dynamical Systems* (Heidelberg: Springer)
- [44] Hirsch M W, Smale S and Devaney R L 2004 *Differential Equations, Dynamical Systems, and an Introduction to Chaos* (Amsterdam: Elsevier)
- [45] Malomed B A 1998 Potential of interaction between two- and three-dimensional solitons *Phys. Rev. E* **58** 7928
- [46] Decker R J, Demirkaya A, Manton N S and Kevrekidis P G 2020 Kink–antikink interaction forces and bound states in a biharmonic ϕ^4 model *J. Phys. A: Math. Theor.* **53** 375702
- [47] Rosas A, Romero A H, Nesterenko V F and Lindenberg K 2007 Observation of two-wave structure in strongly nonlinear dissipative granular chains *Phys. Rev. Lett.* **98** 164301
- [48] Vergara L 2010 Model for dissipative highly nonlinear waves in dry granular systems *Phys. Rev. Lett.* **104** 118001
- [49] Carretero-González R, Khatri D, Porter M A, Kevrekidis P G and Daraio C 2009 Dissipative solitary waves in granular crystals *Phys. Rev. Lett.* **102** 024102
- [50] Merkel A, Tournat V and Gusev V 2011 Experimental evidence of rotational elastic waves in granular phononic crystals *Phys. Rev. Lett.* **107** 225502
- [51] Vorotnikov K, Kovaleva M and Starosvetsky Y 2018 Emergence of non-stationary regimes in one- and two-dimensional models with internal rotators *Phil. Trans. R. Soc. A.* **376** 20170134
- [52] Jackson J D 1999 *Classical Electrodynamics* 3rd edn (New York: Wiley)